Research Article | Vol. 12, No. 1 / 1 January 2021 / Biomedical Optics Express 444
Biomedical Optics EXPRESS

# Highly flexible fiber delivery of a high peak power nanosecond Nd:YAG laser beam for flexiscopic applications

HAMED ABBASI,[1,4] FERDA CANBAZ,[1] RAPHAEL GUZMAN,[2] PHILIPPE C. CATTIN,[3] AND AZHAR ZAM[1,5]

[1]Biomedical Laser and Optics Group (BLOG), Department of Biomedical Engineering, University of Basel, CH-4123 Allschwil, Switzerland
[2]Department of Neurosurgery, University Hospital Basel, CH-4056 Basel, Switzerland
[3]Center for medical Image Analysis and Navigation (CIAN), Department of Biomedical Engineering, University of Basel, CH-4123 Allschwil, Switzerland
[4]hamed.abbasi@unibas.ch
[5]azhar.zam@unibas.ch

**Abstract:** Minimally invasive laser surgeries that require the use of a flexible endoscope (flexiscope) could benefit from high-energy nanosecond laser pulses delivered through fibers for real-time tissue characterization and phenotyping. The damage threshold of the fiber's glass material limits the maximum amount of deliverable peak power. To transmit high-energy pulses without damaging the fiber material, large-diameter fibers are typically used, leading to a limited bending radius. Moreover, in a large-core fiber, self-focusing can damage the fiber even if the tip remains intact. In this work, we tested a fused-end fiber bundle combined with a beam shaper capable of delivering more than 20 MW (>100 mJ/5 ns). The fiber bundle was tested over more than eight hours of operation, with different bending radiuses down to 15 mm. The results demonstrate, to the best of our knowledge, the highest peak power delivered through a flexible fiber, for a frequency-doubled Q-switched Nd:YAG laser.



## 1. Introduction

Q-switched Nd:YAG lasers have been used in industry and medicine for a wide array of applications, including hard and soft tissue ablation [1–4], laser-based diagnosis [5,6], laser-induced breakdown spectroscopy (LIBS) [7–9], laser-induced shockwave measurement [10–12], photoacoustic imaging/tomography [13,14], particle image velocimetry (PIV) [15], nanoparticle synthesis [16–18], laser shock processing [19], spark generation (laser ignition) [20,21] as a feedback mechanism for tissue-specific laser surgery [22–24]. Q-switched Nd:YAG lasers can emit nanosecond pulses at a center wavelength of 1064 nm, with harmonics of 532, 355, 266, and 213 nm. These lasers are also widely used to pump optical parametric oscillators (OPOs) to reach different wavelength regions. For example, photoacoustic imaging/tomography applications could require wavelengths in the 600 to 800 nm region [13,14]. In such applications, laser line mirrors and prisms are typically used to deliver the laser beam to the point of interest. However, this type of free-space delivery is not applicable to remote, standoff, or endoscopic applications. For standoff applications, telescopes are used to deliver and collect light over a long-distance, while remote and endoscopic applications depend on optical fibers for the same purpose. Compared to continuous wave (CW) and pulsed lasers with long pulse durations (milliseconds to microseconds), nanosecond pulses are more challenging to deliver through optical fibers due to their high peak power (the shorter the pulse duration, the higher the peak power). The nanosecond pulses induce more damage caused by laser-driven shockwaves (a result of higher peak energy levels), compared to ultra-short laser pulses (picoseconds to femtoseconds) [25]. The generated shockwaves can

#405825 https://doi.org/10.1364/BOE.405825
Journal © 2021 Received 19 Aug 2020; revised 21 Oct 2020; accepted 2 Nov 2020; published 17 Dec 2020

Biomedical Optics EXPRESS

easily crack the fiber material (glass) [26]. Considering the high peak power of Q-switched lasers (mJ/ns = MW) and the small diameter (cross-section) of optical fibers ($10^{-3}$–$10^{-6}$ $cm^2$), the fiber optic often faces a peak power density (GW/$cm^2$–TW/$cm^2$) that exceeds the laser-induced damage threshold (LIDT) of the glass material. To overcome these challenges, a number of alternatives have been proposed. Sapphire fibers, for example, have a higher LIDT than silica glass fibers. They are, however, more expensive, with a limited choice of length and core size on the market. Additionally, the minimum bending radius (mBR) of a sapphire fiber is much higher than that of a silica fiber with an equal outer diameter. Hollow-core fibers present another possible solution, but they are more suitable for infrared (IR) wavelengths due to the limited smoothness (finesse) of the coating material on the internal surface of the capillary [27]. Other limiting factors of hollow-core fibers include a dramatic increase in attenuation (loss) as it bends [27–29] and optical breakdown (air plasma creation) inside the capillary (bore). To overcome the latter, researchers have experimented with blowing an inert gas with a higher plasma generation threshold into the capillary, and reducing the air pressure by creating a vacuum [29]. While the results showed an improved LIDT, the setup was highly complex (requiring a rotary pump and pressure gage) and bulky, especially at the tip of the fibers, making the technique unsuitable for endoscopic applications.

In glass fibers, damage typically occurs at the facet where air and glass interface. The LIDT of the air-glass interface depends heavily on the polishing quality; therefore, a cleaved fiber is often preferred over polished fiber, especially when a high-quality polishing machine is not accessible [19,30]. The most frequently used method for increasing the LIDT at the air-glass interface is to taper the tip of the fiber and apply an end-cap [31,32]. Applying pressurized air to the fiber tip also helps to remove dust particles that may lead to plasma generation. Placing the coupling optic inside a vacuumed box can also prevent plasma generation, although it increases the complexity of the setup [29]. Another possible means to increase the LIDT is to use large-core optical fibers, up to 1500 µm (the bigger the fiber cross-section, the lesser the need to use a high irradiance, tightly-focused beam for coupling). Different fiber diameters, mBRs, and delivered peak power levels are listed in Table 1. while Table 1 shows that delivering high peak power levels is possible with large core diameter fibers (a potential candidate for remote applications), large core fibers are not suitable for endoscopic applications, where flexibility is imperative. More specifically, increasing the cross-section of the fiber core increases the fiber's tolerance for power; however, it reduces the mBR of the fiber. Therefore, large core fibers cannot be inserted into flexible endoscopes (flexiscopes). An alternative approach would be to bundle fibers with a cross-section large enough to prevent the use of tightly focused beams for coupling, and a combined fiber diameter small enough to maintain bending capabilities. Fiber bundle diameters can be adjusted depending on the needs. A few studies have shown that delivering nanosecond pulses with thick fiber bundles (up to 5, 8, or 9 mm diameter) is possible [13,33–35]. Another benefit of using fiber bundles is that light cannot travel between the fibers within a bundle, thereby preventing self-focusing.

In general, the output intensity profile of a laser has a Gaussian intensity distribution. In the case of fiber coupling, the Gaussian profile of the laser can induce a hot spot a few millimeters after the fiber facet mainly due to the high intensity of the reflected beam at the center of the fiber [15]. Therefore, to avoid related damages, it is necessary to homogenize the laser beam profile. Homogenization can be achieved using a lenslet array (spherical/cylindrical) or a diffractive optical element (DOE). A homogenized beam (ideally top-hat-shaped) can prevent self/re-focusing (also known as self/re-imaging) inside the fibers. It is worth mentioning that the distribution of a Gaussian input beam might be altered at the bundle's output for non-ordered bundles, while this is not the case for top-hat beams. For this reason, large-core fibers are mostly used in combination with a beam homogenizer [14,19,49]. Beam shaping can also help to obtain a uniform ablation crater, which is required for some applications. The crater produced by the

Biomedical Optics EXPRESS

**Table 1. Delivered peak power and estimated mBR for different fiber diameters[a].**

| λ [nm] | Type | Core | $r_{core/clad/bundle}$ [μm] | Estimated mBR [mm] | Power [MW] (E/τ) [mJ/ns] | Assisted by | Work |
|---|---|---|---|---|---|---|---|
| **1064** | single | solid | 100/-/- | 10–31 | 0.5 (3/6) | - | [36] |
| | | | 100/120/- | 12–36 | 2.3 (16/7) | DOE | [37] |
| | | | 200/-/- | 21–62 | 2.5 (15/6) | - | [36] |
| | | | 275/-/- | 28–85 | 3.3 (30/9) | - | [30] |
| | | | 300/-/- | 31–93 | 4.7 (70/15) | taper | [31] |
| | | | | | 15 (120/8) | taper | [32] |
| | | | 400/-/- | 41–124 | 3.5 (35/10) | - | [38,39] |
| | | | | | 5.3 (80/15) | taper | [31] |
| | | | 470/-/- | 48–145 | 7.5 (45/6) | - | [36] |
| | | | 500/-/- | 52–155 | 2.1 (12.5/6) | vacuum box | [40] |
| | | hollow | 350/-/- | 36–108 | 2.9 (21.5/7.5) | - | [41] |
| | | | | | 5.9 (47/8) | He | [20] |
| | | | 500/750/- | 75–225 | 4.3 (30/7) | - | [27] |
| | | | 500/-/- | 52–155 | 5 (30/6) | - | [21] |
| | | | | | 8.3 (50/6) | He | [42] |
| | | | | | 9.8 (142/14.5) | - | [28] |
| | | | | | 17.6 (158/9) | vacuum cell | [29] |
| | | | | | 20 (100/5) | - | [43] |
| | bundle | solid | -/-/4500 | - | 16 (80/5) | - | [13] |
| | | hollow | 350/430/2750 | 45–131 | 24 (145/6) | - | [44] |
| | | | | | 33 (200/6) | $N_2$ | [45] |
| **532** | single | solid | 500/517.5/- | 52–155 | 1.3 (12.8/10) | - | [46] |
| | | | 500/-/- | 52–155 | 3.4 (24/7) | - | [47] |
| | | | | | 4.1 (29/7) | - | [48] |
| | | | 750/-/- | 77–232 | 20 (100/5) | lens array, $N_2$ | [19,49] |
| | | hollow | 500/-/- | 52–155 | 10 (50/5) | - | [43] |
| | | | | | 10.7 (75/7) | He | [50] |
| | bundle | solid | 100/110/550 | 11–33 | 3.1 (25/8) | DOE | [15] |
| | | hollow | 350/430/2750 | 45–131 | 10 (70/7) | - | [51] |
| | | | | | 17.5 (105/6) | $N_2$ | [45] |
| **355** | single | hollow | 500/-/- | 52–155 | 0.29 (2/7) | He | [50] |
| **266** | single | hollow | 500/-/- | 52–155 | 0.14 (1/7) | He | [50] |
| | | | | | 3 (15/5) | - | [43] |
| **OPO** | single | solid | 500/517.5/- | 52–155 | 12 (48/4) | lens array | [14] |
| | | | 750/775/- | 78–233 | 15 (60/4) | lens array | [14] |
| | bundle | solid | 92.5/100/4000 | 14.3–34.3 | 6.4 (32/5) | - | [35] |

[a]A hyphen (-) indicates that a parameter is not applicable or was not mentioned in a study. Estimated mBR ranges derived based on the method described in Sections 2.2 and 2.3 (for unknown cladding radiuses, the radius of the core plus 3 % has been used for calculations). The method for estimating mBR is more accurate for solid core fibers than for hollow-core fibers.

Biomedical Optics EXPRESS

top-hat laser beam is much smoother and flatter than that produced by the traditional Gaussian beam. Besides, it has recently been shown that using a homogenized beam for LIBS reduces the plasma shielding and matrix effect, improves the signal intensity and repeatability due to uniform beam energy distribution, and results in less unwanted heating [52,53]. When using a Gaussian beam for launching fiber bundles, fibers located in the central part of the bundle encounter more power than those located in the outer part. Therefore, while centrally located fibers might incur damage, the outer fibers can still deliver power. In this study, we report on the use of a fiber bundle in combination with a top-hat beam shaper for flexible delivery of second harmonic pulses of a Q-switched Nd:YAG laser beam.

## 2. Materials and methods

### 2.1. Fiber material

In our experiments, we used an incoherent silica fiber bundle. Silica is the most widely-used material for optical fibers, mainly because of its flexibility and availability and because it costs less than other fiber materials. Moreover, as compared to other glass materials, e.g., borosilicate glass (BK7), fused silica does not demonstrate any correlation between the number of shots and LIDT, due to its short lifetime decay from the conduction band to the valance band [54,55]. Low OH silica (below one ppm) was selected as the fiber's core material (CeramOptec GmbH, Bonn, Germany). Fluorine-doped (F-doped) silica made up the cladding material. No buffer was provided. Four different jacket materials were available, each with different operating temperatures: polyimide (−190 to +350 °C), ethylene tetrafluoroethylene (also known as ETFE) (−40 to +150 °C), nylon (−40 to +100 °C), and acrylate (−40 to +85 °C). Of these, polyimide was selected due to its higher operating temperature.

### 2.2. Bending radius

Glass fibers have a limited bending radius. Under a tight bend, the inner and outer surfaces of the fiber experience high compression and strong tension, respectively. Strong tension on the glass' surface causes crack growth and, subsequently, fracture. To avoid this problem, a minimum bending radius (mBR) is defined to determine the bending limit of a fiber. Bending the fiber below this limit might result in a broken fiber. The bending limit or mBR is determined by fiber specific parameters:

$$mBR = k.r \tag{1}$$

where, $k$ is a specific fiber material parameter and $r$ is the outer radius of the cladding. Here, k is defined as a ratio as follows:

$$k = \frac{Y}{\sigma} \tag{2}$$

where $Y$ is the Young's modulus of the fiber material, and $\sigma$ is the highest amount of tension that the fiber experiences at the outer surface of the bend [56,57]. Young's modulus for silica-based glass is equal to 72 GPa (=10,440 kpsi). The fiber material used in this study has a standard proof test of 70 kpsi (measured by the manufacturing company). Therefore, parameter $k$ was calculated to be 149.14. However, the fiber might survive for a short period with a bending radius below this limit. Even so, the breaking radius is larger while the fiber is run with lasers, especially with high-power lasers. For instance, Sun et al., found that the strength of their fiber diminished by approximately 2 to 3 times after applying a high-power laser. For silica-based fibers, the parameter $k$ typically ranges between 80 and 110 for short-term mBR, and between 160 and 300 for long-term mBR; the higher the applied power, the higher the $k$ parameter (indicating a decrease in strength). The short-term bending radius is defined as a mechanical stress limit, meaning that the fiber might be irreversibly damaged or even broken if subjected to a bending radius lower than the one defined. Likewise, fibers should not be held at the short-term mBR

Biomedical Optics EXPRESS

limit for more than 60 seconds. Long-term mBR is defined as the limit before causing damage to the fiber; however, bending loss may be high as the fiber approaches the long-term mBR. For the purchased silica fiber, the manufacturer determined that k=100 and k=300 for short-term and long-term mBR (while working with high-power lasers), respectively.

### 2.3. Fiber bundle

Like a stranded wire that can be bent more easily than a solid wire with the same diameter, a fiber bundle has a much smaller mBR than a single fiber with the same diameter. To estimate the mBR of a fiber bundle, the following equation can be used:

$$mBR' = mBR + r' - r \tag{3}$$

where $mBR'$ and $mBR$ represents the mBR of the fiber bundle and that of the individual fibers used to develop the bundle, respectively; $r'$ and $r$ represents the radius of the fiber bundle and of the individual fiber, respectively. As shown in Eq. (3), adding several individual fibers beside each other do not add up to the mBR more than the bundle radius. Figure 1 illustrates the difference between the mBR of an individual fiber versus that of the fiber bundle.

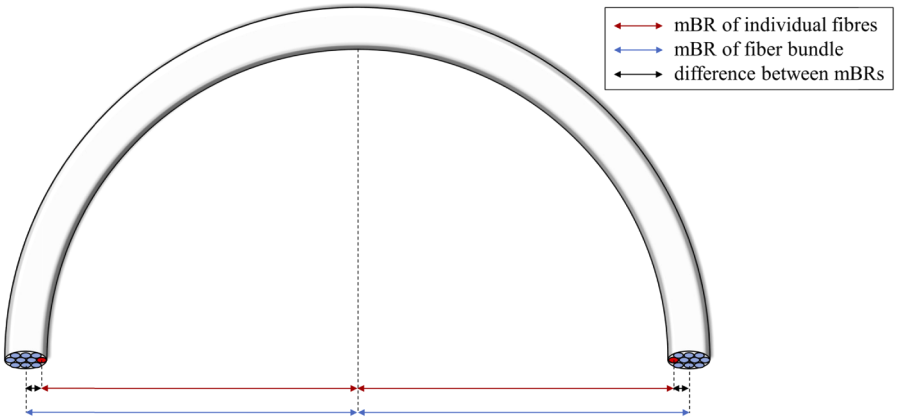


**Fig. 1.** The difference (black arrow) between the mBR of a single fiber (red arrow) and that of a fiber bundle (blue arrow).

As shown in Fig. 1, the difference between the mBR of a single fiber and that of a fiber bundle is less than the radius of the bundle. Therefore, by utilizing a fiber bundle, the cross-section of the fiber can be increased while keeping the mBR short. To find the ratio between the mBR of a fiber bundle and the mBR of a single fiber with the same radius as the fiber bundle, irrespective of the radius of the fibers in the bundle, a packing problem must be solved. In mathematics, the packing problem is used to determine how many circles (with the same radius) can fit into a bigger circle by minimizing the space between the circles. In other words, solving the packing problem finds the most compact arrangement for a defined number of neighboring circles of the same size, for which the geometry of that group of circles is similar to another big circle. There is no unique equation that can determine the ratio between the radius of packed circles and that of the surrounding circle; there is only a conjectured upper bound, as introduced by David W. Cantrell [58]. Employing Cantrell's upper bound, we have:

$$f_n = \frac{r}{r'} \leqq \frac{4\rho}{4\rho - 1 + (16\rho^2 + (16n - 24)\rho + 1)^{1/2}} \tag{4}$$

where $f_n$ is the fraction describing the ratio of the surrounded circle to the surrounding circle, $n$ is the number of individual fibers used to develop the bundle, and $\rho$ is the density of an infinite

Biomedical Optics EXPRESS

hexagonal packing of circles:

$$\rho = \frac{\pi}{2(3)^{1/2}} \approx 0.91 \tag{5}$$

However, for a few $n$, Cantrell's conjectured upper bound has been violated [58]. Since 1967 [59], the packing problem for $n$ number of surrounded circles has been solved and improved upon by different research groups [60,61]. A database hosted by Otto von Guericke University Magdeburg provides answers to packing problems up to N=2600 [58]. By using the best-known packings of equal-sized circles within a circle as given by the database, a fraction of surrounded circle radius to the surrounding circles radius, $f_n$, can be assessed.

Combining Eqs. (1), (3), and (4) we derive:

$$\frac{mBR''}{mBR} = k(f_n(k-1)+1)^{-1} \tag{6}$$

Here, $mBR''$ represents the minimum bending radius of a fiber that has the same radius as a bundle with a minimum bending radius of $mBR$. Employing Eq. (6) improvement of mBR by using $n$ number of individual fibers in a bundle is calculatable, irrespective of the radius of fiber or bundle. Figure 2 shows the improvement in mBR for k=100 (short-term) and k=300 (long-term) for different numbers of individual fibers in a bundle.

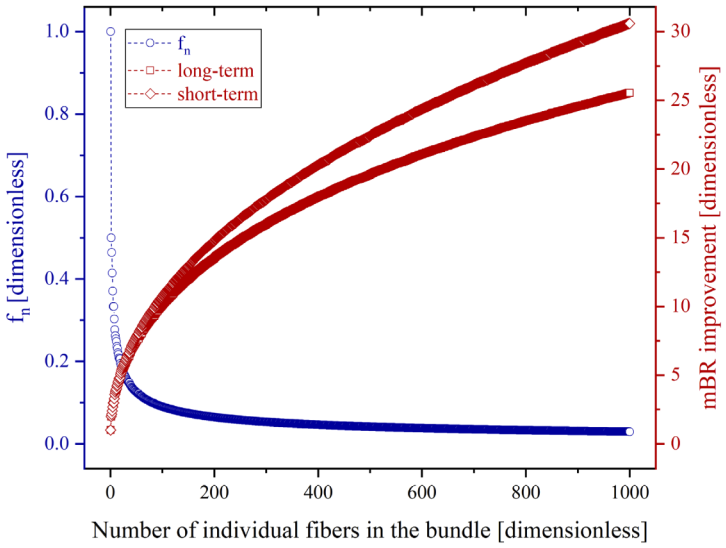


**Fig. 2.** The fraction of individual fiber radius to bundle radius ($f_n$), and mBR improvement (long-term and short-term) for a bundle of $n$ individual fibers.

In this study, an 800 m long multimode fiber was divided into 800 pieces of 1 m long fiber pieces to make the bundle. Both ends were polished to 0.3 µm specification (performed by the manufacturing company). Therefore, as shown in Fig. 2, the short- and long-term mBRs were 24 and 28 times smaller, respectively, than a single fiber of the same radius as the bundle.

Even though the use of fiber bundles over single large-diameter fibers is highly advantageous in terms of mBR, the coupling efficiency (i.e., that ratio of the coupled energy to the incident energy) of a fiber bundle is less than that of a single fiber. Two main reasons account for the reduced coupling efficiency. First, in a single fiber, the light is focused on the core area, while in a fiber bundle, the light faces both the core and cladding area of individual fibers in the bundle. At the tip of the bundle, plastic/polymer parts, like the jacket, are detachable, but the cladding is made of glass and cannot be separated from the core before fusing. Therefore, thin cladding

Biomedical Optics EXPRESS

is desirable to reduce the cross-section of cladding at the tip of the bundle. In this study, the individual fibers used to develop the bundle had a core and cladding radius of 50 µm and 53 µm, respectively. Second, the gap between the fibers also reduces coupling efficiency. The ratio of the glass area to the gap area in the tip of a bundle is called density or fill factor. Based on the number of individual fibers in the bundle, the density may differ. To reach a higher filling factor, the number of fibers can be increased. However, based on the number of individual fibers in the bundle, a few loose fibers are to be expected. Without loose fibers, wrapping the individual fibers would be enough to fix the position of the fibers in the bundle. For instance, Stephens et al. developed a bundle of 19 fibers, and managed to fix the fibers by mechanically holding them in a close-fitting tapered glass capillary tube [15]. However, in most cases, a few loose fibers are likely. Figure 3 shows the density and number of loose fibers based on the number of individual fibers in the bundle. A horizontal line, demonstrating the density limit, acquired from Eq. (5), is depicted in Fig. 3 as well.

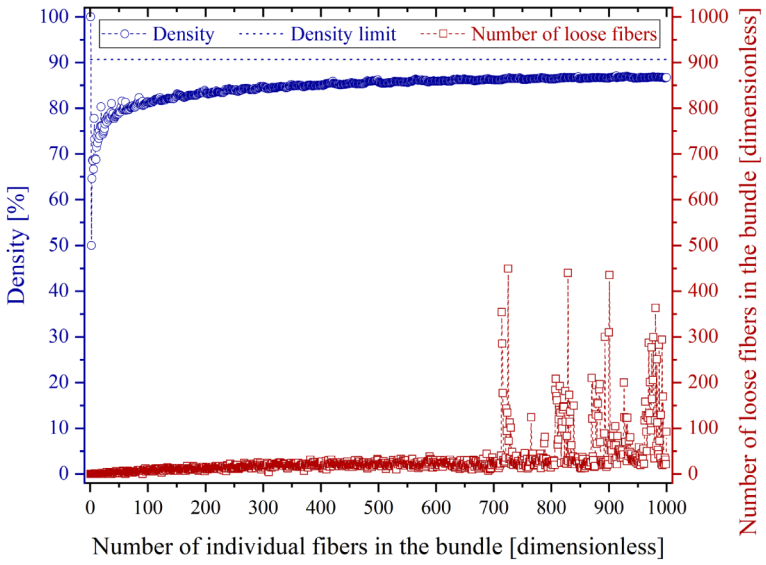


**Fig. 3.** Theoretical density and number of loose fibers for packing of $n$ individual fibers.

Since light cannot travel over a long distance in the cladding, and also considering the limitation of a fiber bundle's density, the following equation can be used to estimate the coupling efficiency of the bundle:

$$\textit{Bundle coupling efficiency} \leqq \rho\left(\frac{r_{core}}{r_{clad}}\right)^2 \tag{7}$$

where $\rho$, $r_{core}$, and $r_{clad}$ represent the density, the radius of the core, and the radius of the cladding, respectively. Since the light will be sent through the central part of the fiber bundle and because gaps exist in the outer part of the bundle, we can consider the maximum density of a hexagonal packing of circles [Eq. (5)]. Equation (7) determines a coupling efficiency of approximately 81% or less from our fiber bundle. Figure 4 represents a simulation of a bundle of 800 fibers, packed with the most compact known geometry. In this configuration, the fibers have 1,746 contacts, 95 of which have contact with the container (the outer circle); however, 23 loose fibers exist, and are depicted in gray in Fig. 4. The density of this configuration is 0.86, and it has an $f_n$ value of 0.033 [58].

Due to the existence of loose fibers (fibers that still have a degree of freedom for movement inside the container; so-called rattlers) in the bundle, holding the 95 boundary fibers would not

Biomedical Optics EXPRESS

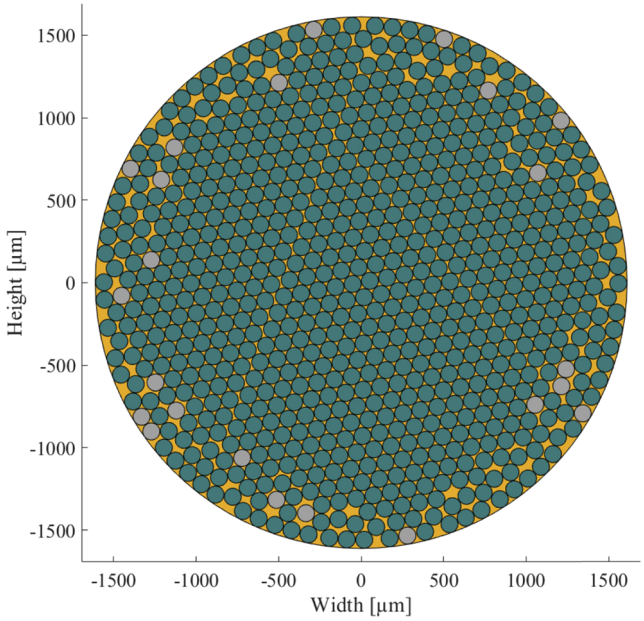


**Fig. 4.** Simulation of packing 800 individual fibers with a radius of 53 µm ($r_{clad}$) in a circle (capillary container). The fibers with a degree of freedom for movement are colored in gray. The yellow zone shows the wasted areas (approximately 14 % without fusion).

be enough to fix them. At the output facet, the fibers could be glued to each other, but this would not work for the input facet (subjected to high peak power pulses), due to the low LIDT of glues. Therefore, at the input facet, fibers were fused to each other (jackets removed). Fusing the fibers also served to increase the density by filling the gaps between fibers. During the fusing process (performed by the manufacturing company), the fibers attained a hexagonal shape. Filling the gaps reduced the outer diameter of the bundle as well.

### 2.4. Output energy measurement

To measure laser energy, a high damage threshold energy meter (EnergyMax-USB J-50MB-YAG, Coherent Inc., United States), was used, depicted as EM in Fig. 5. The delivered energy was measured directly by placing the EM in front of the fiber bundle.

### 2.5. LIDT measurement

To determine the bundle's LIDT, we utilized the second harmonic of a Q-switched flashlamp-pumped Nd:YAG laser (Q-Smart 450, Quantel, France) with a pulse duration of 5 ns providing a Gaussian beam output ($M^2$ below 2). For this part of the experiment, a single convex lens (indicated as FL in Fig. 5) was used for focusing (i.e., no beam shaper (BS) or aperture (A) was used). The laser's energy was gradually increased by reducing the delay between the flashlamp and Q-switch until damage was observed. A longwave infrared (LWIR) thermal camera (FLIR A655sc, FLIR Systems AB, Sweden) was initially used (depicted as TC in Fig. 5) in the setup; however, it was later removed as it failed to record any temperature change when damage occurred. This thermal camera shows the average recorded thermal radiation (accumulated heat) over each frame (tens of ms), while damage occurs within the range of laser pulse duration (ns), hence temperature change at the moment of damage could not be recorded. By obtaining the LIDT for a specific beam parameter, LIDT for another beam specification (close to the original one) can be

Biomedical Optics EXPRESS

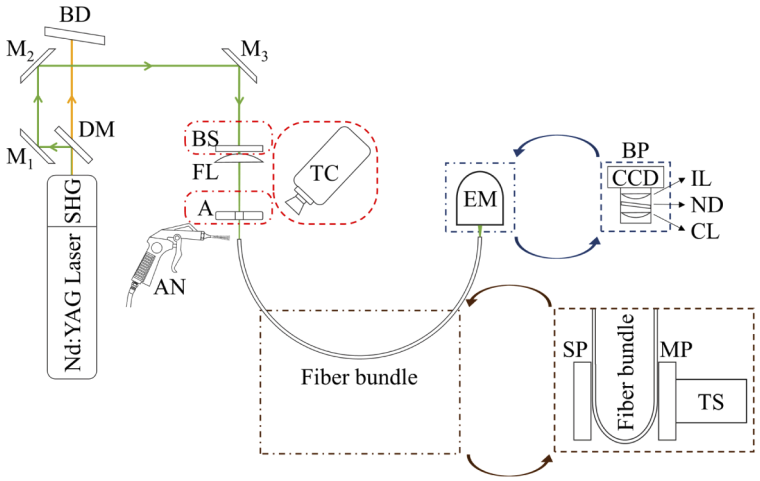


**Fig. 5.** Schematic of the experimental setup. Parts inside dash-dotted rectangles have been replaced with parts inside dashed rectangles of the same color during different parts of the experiment. Components inside red rectangles with rounded corners were present in some parts of the experiment only. SHG: Second Harmonic Generator, DM: Dichroic Mirror, M: Mirror, BD: Beam Dump, BS: Beam Shaper, FL: Focusing Lens, A: Aperture, AN: Air Nozzle, TC: Thermal Camera, SP: Stationary Plate, MP: Moving Plate, TS: Translation Stage, EM: Energy Meter, BP: Beam Profiler, CCD: Charge-Coupled Device, IL: Imaging Lens, ND: Natural Density filter, CL: Collimating Lens.

estimated using the following equation:

$$LIDT_{(\lambda_2,\tau_2,PF_2)}\left[\frac{J}{cm^2}\right] \approx LIDT_{(\lambda_1,\tau_1,PF_1)}\left[\frac{J}{cm^2}\right] \times \left(\frac{\lambda_2}{\lambda_1}\right)^{j_\lambda} \times \left(\frac{\tau_2}{\tau_1}\right)^{j_\tau} \times \left(\frac{PF_2}{PF_1}\right) \quad (8)$$

where $\lambda$ is the wavelength, $\tau$ is pulse duration, and $PF$ is the profile factor. In most cases, $j_\lambda$ and $j_\tau$ can be approximated as 1 and ½, respectively; however, a few studies have reported different numbers [26,54,62,63]. $PF$ represents the homogeneity of the beam profile. As a rule of thumb, a top-hat-shaped laser beam has a $PF$ approximately two times better than that of a typical laser with a Gaussian intensity distribution. In a Gaussian distribution, the percentage of photons within a band around the mean, four standard deviations wide (2σ on either side of the mean), is around 95%. Assuming a rectangular top hat (in a two-dimensional plane), a top-hat beam with the same width (2σ from either side of the mean) and only half the height of the Gaussian distribution would encompass the same number of photons (assuming 5% loss for top-hat beam shaper) as the Gaussian beam. Therefore, individual fibers at the center of a bundle illuminated with a Gaussian laser beam have a two times higher chance (than average) of being damaged. Contrastingly, with top-hat illumination, most of the individual fibers tolerate the same amount of energy. In sum, by converting the laser beam from Gaussian to top-hat, we can expect a two-fold increase in the bundle's ability to handle power.

### 2.6. Beam shaping

We used a high damage threshold top-hat beam shaper, GTH-5-250-4-532 (TOPAG Lasertechnik GmbH, Darmstadt, Germany), with an antireflection coating at 532 nm. The beam shaper had an integrated lens with a 250 mm focal length. It required an input beam with a diameter ($1/e^2$) of approximately $5.0 \pm 0.15$ mm, $TEM_{00}$.

The beam shaper's free-form surface redistributed a top-hat square beam with beam homogeneity of ±5 % (in reference to the average intensity within the top-hat beam) and a size of

Biomedical Optics EXPRESS

$4 \times 4\,mm^2$ (scalable with an additional lens) at its focal length. Since the top-hat size created exceeded the diameter of the fiber bundle, an additional lens with a 500 mm focal length was placed after the beam shaper to adjust the size of the top-hat beam. The beam shaper has been shown as BS in Fig. 5. The following equations show the working distance and top-hat beam size of the beam shaper in combination with an additional lens.

$$working\ distance \approx \frac{f_i f_a}{f_i + f_a} \tag{9}$$

$$top\ hat\ size\ [mm] \approx 4\frac{working\ distance}{f_i} = 4\frac{f_a}{f_i + f_a} \tag{10}$$

In Eqs. (9) and (10), $f_i$ is the integrated focal length (250 mm), and $f_a$ is the focal length of the additional lens (500 mm). However, using an input beam with a larger diameter results in a larger top-hat output at a slightly shorter working distance, with rounded corners/edges. A round diaphragm was used to aperture and change the profile of the beam from square to round before entering the fiber bundle.

Another benefit of using a beam shaper to couple the light into the fiber (compared to a single-lens setup) is that it enters the fiber with a very low numerical aperture (NA). Launching a fiber with a low NA (low incidence angle) results in filling the fiber with low-order modes, also known as an underfilled launch condition. Low-order modes are less sensitive to bending than high-order modes as the total internal reflection (TIR) angle is not close to the critical angle of the fiber. Therefore, by changing the critical angle of the fiber during bending, the TIR condition is still fulfilled. More information is provided in Section 2.8.

### 2.7. Beam profiling

A custom beam profiler was used to observe the profile of the laser at the fiber output. The setup consisted of a collimating lens, a natural density filter, an imaging lens, and a megapixel CCD. The setup of the beam profiler is shown as BP in the delineated experimental setup shown in Fig. 5. The beam profiler, depicted in a blue dashed rectangle, was replaced with the energy meter (EM), shown inside the dash-dotted blue rectangle, after the profiling experiments.

### 2.8. Durability and bending loss measurement

To maximize the repeatability of any laser experiment, keeping the laser power constant throughout the experiment is vital. Therefore, for potential flexiscopic applications, the power of the laser is required to remain constant while the fiber is under different bending radiuses. Thus, we simulated whether the developed fiber is bend-sensitive or bend-insensitive. Next, the simulation has consequently been supported by the experiment.

Light delivery inside solid core waveguides is based on total internal reflection, thus, bending loss occurs only if the light inside the fiber core cannot be reflected back from the cladding to the core. Based on the refractive index of the core and cladding, a critical angle is defined for guidance. Hence, the fiber can deliver light rays propagated into the core below the critical angle, which limits the incidence angle of the light entering the fiber. The critical threshold for the incidence angle is called the acceptance angle (see Fig. 6). Alternatively, NA can also be used to assess the acceptance angle. The critical angle ($\theta_{crit}$), acceptance angle ($\theta_{acc}$), and NA of fibers are related to the refractive index of the core ($n_{core}$) and of the cladding ($n_{clad}$), according to the following equations:

$$\theta_{crit} = \sin^{-1}\left(\frac{n_{clad}}{n_{core}}\right), \quad NA = n_{out}\sin\theta_{acc} = (n_{core}^2 - n_{clad}^2)^{\frac{1}{2}} \tag{11}$$

where $n_{out}$ is the refractive index of the fiber's outside environment. Figure 6 illustrates the definition of $\theta_{crit}$ and $\theta_{acc}$.

Biomedical Optics EXPRESS

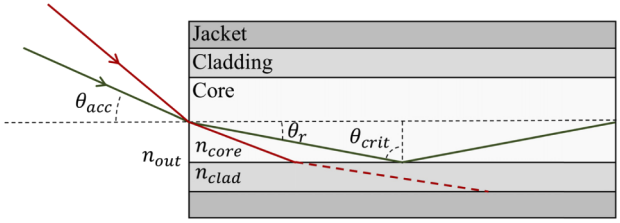


**Fig. 6.** A beam entering the fiber with an angle equal to or below $\theta_{acc}$ refracts at angle $\theta_r$, and reflects from the core-cladding interface with an angle equal to or greater than $\theta_{crit}$ (complementary angle of $\theta_r$). Beams outside of these boundary limits (e.g., red beam in the figure) would not be able to follow TIR and will be absorbed by the jacket (if the fiber has one).

Since all parameters mentioned in Eq. (11) are wavelength-dependent, they need to be known for the wavelength of the employed laser (532 nm). The fiber core and cladding were silica glass (also known as silicon dioxide, $SiO_2$), and F-doped silica, with refractive indexes of 1.457 and 1.440 (at 632.8 nm), respectively. The NA was 0.22 at the standard helium-neon (He-Ne) laser wavelength (632.8 nm). The Sellmeier dispersion equation [64] can be used to model the refractive index of silica at the center wavelength of the laser (532 nm):

$$n(\lambda) = \left(1 + \sum_{i=1}^{M} \frac{B_i \lambda^2}{\lambda^2 - C_i}\right)^{\frac{1}{2}}, \begin{pmatrix} B_1 & C_1 \\ B_2 & C_2 \\ B_3 & C_3 \end{pmatrix}_{silica} = \begin{pmatrix} 0.6961663 & 0.0684043^2 \\ 0.4079426 & 0.1162414^2 \\ 0.8974794 & 9.8961610^2 \end{pmatrix} \tag{12}$$

where $\lambda$ [μm] is the wavelength, and $B_i$ [dimensionless] and $C_i$ [$\mu m^2$] are experimentally measured Sellmeier coefficients; the three-term (M=3) equation yields an absolute residual in the order of $10^{-6}$ at 20° C [65]. Employing Eq. (6), $n_{core}$ at 532 nm was calculated to be 1.460. A next step was to estimate $n_{clad}$ at 532 nm. Based on the percentage of the doped fluorine, the refractive index varies from the pure silica; the higher the dopant percentage, the lower the refractive index [66]. The percentage of fluorine dopant can be estimated through the following equation, with an accuracy greater than $10^{-4}$ [67]:

$$d_F(\lambda) = \frac{n_{silica}(\lambda) - n_F(\lambda)}{4.665.10^{-3}} \tag{13}$$

where $d_F(\lambda)$ is expressed in [Mol %]. By solving Eq. (7), with refractive index data for the He-Ne wavelength, and subsequently with the achieved dopant percentage and core refractive index for the frequency-doubled Nd:YAG wavelength, the cladding refractive index at 532 nm was estimated to be 1.443. The next step was to find the change in the refractive index while the fiber bends. The refractive index of a fiber core/cladding under a certain bending radius (BR) can be determined by the following equation [68–70]:

$$n_{bent} = n_{straight}\left(1 + (1 + \chi)\frac{x}{BR}\right) \tag{14}$$

where $\chi$ is an elasto-optic parameter equal to −0.22 [dimensionless] for silica material [68–70], and $x$ [expressed in the same dimension as $BR$] is the transversal distance from the center of the core cross-section, positive outwards and negative towards the center of curvature. Figure 7 shows the acceptable NA (upper limit), $\theta_{acc}$ (upper limit), and $\theta_{crit}$ (lower limit) for different BRs.

According to the simulation depicted in Fig. 7, at long-term BR (k=300) incident beams with NAs greater than 0.20 (incident angle greater than 11.5 degrees) would not be guided through the

Biomedical Optics EXPRESS

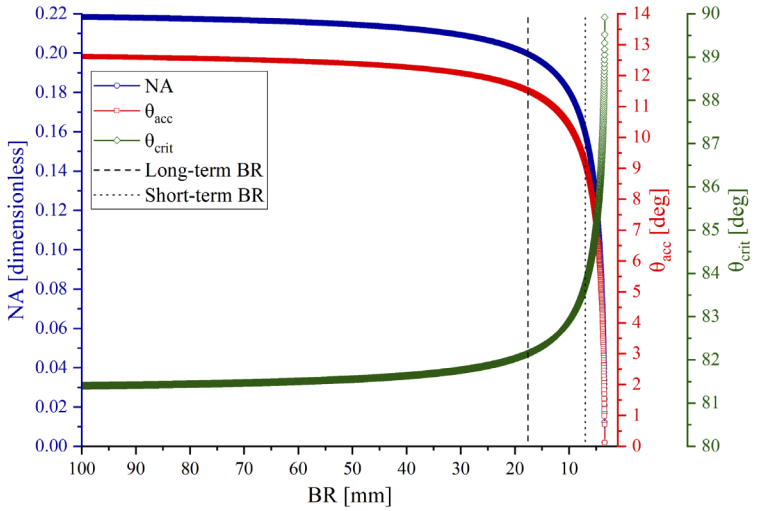


**Fig. 7.** Acceptable NA (upper limit), $\theta_{acc}$ (upper limit), and $\theta_{crit}$ (lower limit) for different BRs, including long-term (k=300) and short-term (k=100) BRs.

bent fiber due to increased $\theta_{crit}$ (82.1 degrees). Similarly, for short-term BR (k=100) the limiting NA is 0.16 and also the limiting incident and critical angles are 9.2 and 83.7 degrees, respectively. Figure 7 clearly shows that the bending loss depends strongly on the launch condition. Due to the very low NA launch condition employed in this study, no bending loss was expected.

To evaluate the durability of the fiber bundle, the laser operated for one hour at 1 Hz (3600 pulses) while the fiber was bent into a half-circle. Each pulse of delivered energy was recorded with the energy meter connected to a computer. The above-mentioned durability evaluation experiment was repeated three times.

To measure the bending loss, the fiber bundle was placed between two plates; the first plate was attached to the optical table, and the second one was attached to a motorized stage (8MT167S-25LS, Standa Ltd., Lithuania) moving with a step size of 100 µm (dashed brown box in Fig. 5). The following procedure was repeated three times: first, the fiber bundle was configured to the long-term mBR (17.6 mm) and kept at the same position while the laser operated at 1 Hz for 1 hour (3600 pulse measurements). Then, as the BR was adjusted from 17.6 to 15.0 mm, with a step size of 100 µm, 100 pulses were delivered through the fiber bundle at each step. A bending radius of around 15 mm has been reported as a necessary bending radius for endoscopic applications [71]. Each pulse of delivered energy was recorded with the energy meter connected to a computer.

## 3. Results and discussion

### 3.1. Fiber bundle

Figure 8 shows the fiber bundle input cross-section as captured by a fiber inspection scope (FS201, Thorlabs Inc., United States) manually connected to a cellphone camera.

Filling the gaps (during the fusion process) between the individual fibers increased the density and, consequently the coupling efficiency. Likewise, the profile (cross-section shape) was changed from circular to semi-hexagonal, particularly for the fibers far from the center of the bundle.

Biomedical Optics EXPRESS

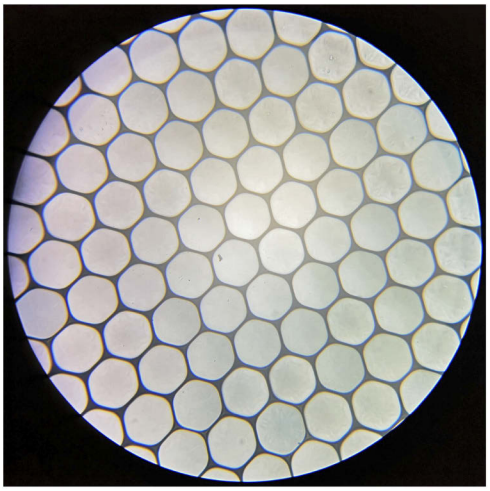

**Fig. 8.** Image of fiber bundle input cross-section as captured by a fiber microscope, with a field of view (FoV) of approximately 600 µm.

### 3.2. LIDT measurement

Our first attempt to examine the fiber bundle made use of a single convex lens focusing (FL in Fig. 5) setup, while the fiber was bent into a half-circle (brown dash-dotted box in Fig. 5) with a BR=318.3 mm. To avoid laser-induced air breakdown, a long focal length lens (f=75 cm) was utilized (the higher the focal length, the bigger the focal spot). To increase the beam size at the fiber input, the fiber tip was placed 18.8 cm after the focal spot, filling approximately half of the fiber bundle end face. While an air nozzle was applied to the tip of the fiber input and a thermal camera monitored the tip, the energy of the laser was gradually increased until damage was observed. The damage occurred at an input peak power of 15.52 MW (77.6 mJ/5 ns), while the output power was 12 MW (60 mJ/5 ns), with a Gaussian beam profile. These numbers correspond to a delivery efficiency of 77.3 %. Using the beam spot size at the fiber input, the damage threshold was calculated to be 0.87 GW/cm$^2$ (Gaussian, 532 nm, 5 ns). Given the slightly lower LIDT of F-doped silica, compared to pure silica [72], we assume that the damage originated from the cladding. Figure 9 shows the fiber input after being damaged.

The bundle was sent back to the manufacturer for repair, the thermal camera was removed from the setup (as it did not record any temperature change), and last but not least, a beam shaper (to homogenize the beam profile) and an aperture (to change the beam profile from square to round) was added to the setup. The fiber bundle was 5 cm shorter after repair. Therefore, the remaining experiments were carried out using a 95 cm fiber bundle.

### 3.3. Beam profiling

To profile the beam at fiber output, a custom-made beam profiler (BP in Fig. 5) replaced the energy meter (EM in Fig. 5) in the experimental setup. Beam profiling was performed with low energy to avoid ablating the CCD while the fiber was bent (BR=302.2 mm) into a half-circle (brown dash-dotted box in Fig. 5). Figure 10 shows the difference between the profile of the fiber bundle output beam without and with using a top-hat beam shaping setup placed before the fiber bundle.

As evident in Fig. 10, no hot zone was captured when the top-hat beam shaper was employed.

Biomedical Optics EXPRESS

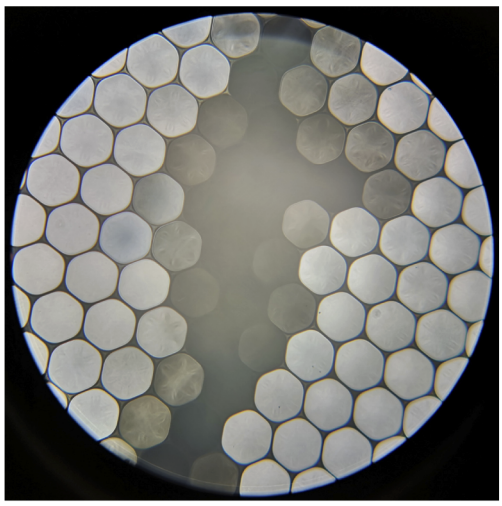

**Fig. 9.** Image of the fiber input after being damaged (FoV≈600 µm).

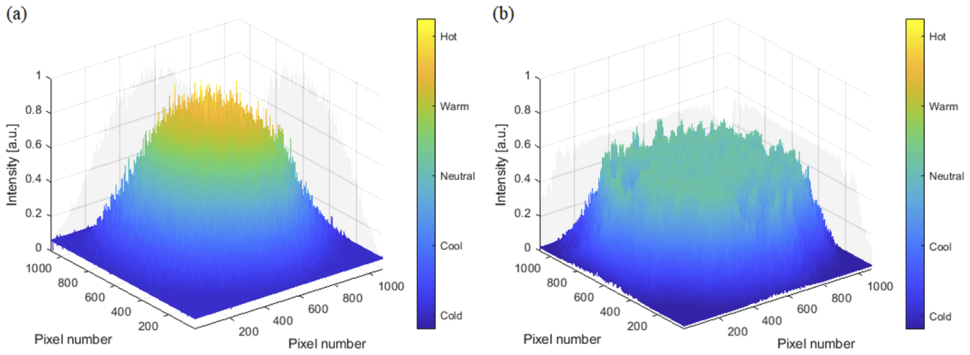


**Fig. 10.** Profile of fiber output beam without (a) and with (b) top-hat beam shaper. For each beam profile, ten different measurements were averaged. The Gaussian and top-hat beam measurements had a relative standard deviation of 8.3% and 5.8%, respectively.

### *3.4. Durability and bending loss measurement*

Figure 11 shows the durability and bending loss measurements for three consecutive measurements (a, b, and c).

For each repetition, while the bending radius was reduced from 302.2 mm (first hour) to 17.6 mm (second hour), no significant reduction in the delivered power was observed. The average energy ± standard deviation (SD) measured for the half-circle BR was 102.6 ± 3 mJ. This output energy was achieved while the input energy to the bundle was 133 mJ (coupling efficiency of 77.1 %). Note that many laser parameters (e.g., beam profile, beam NA, and beam size at the bundle input) and also bundle properties (e.g., acceptable NA, gaps between fibers, reflection properties) can affect the coupling efficiency. An antireflection coating at the input facet of the fiber bundle could further improve the coupling efficiency. The average energy ± SD measured for the long-term mBR was 100.2 ± 3.1 mJ, and lastly the average energy ± SD measured for BRs smaller than the long-term mBR was 97.6 ± 3 mJ.

Considering the fluctuations in the output energy of the laser, the repeatability of the energy meter and consequently the high uncertainty of the measurements, no precise relation between

Biomedical Optics EXPRESS

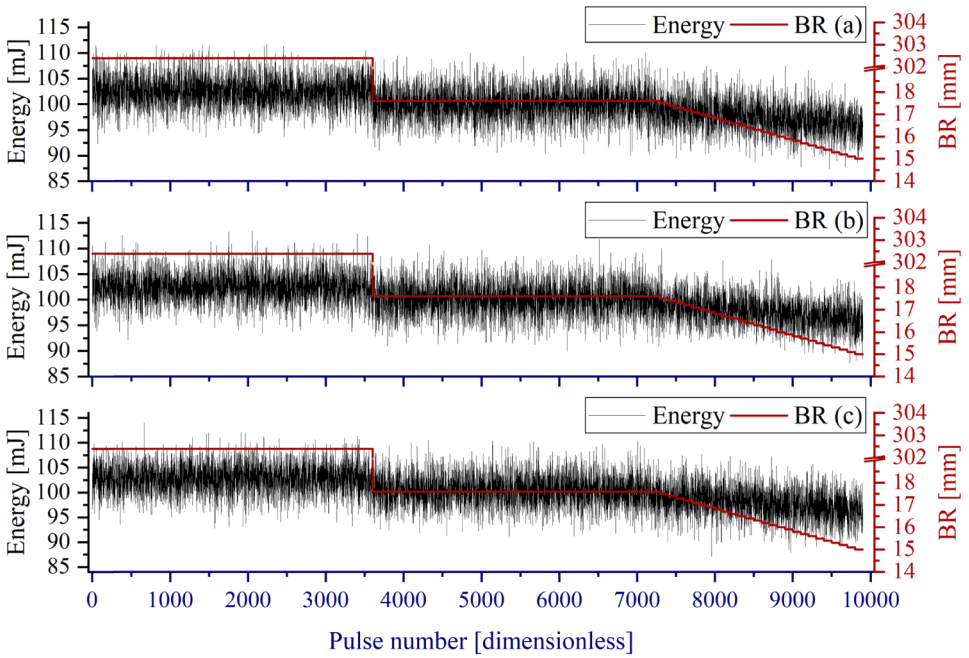


**Fig. 11.** Three repeated (a, b, and c) output energy measurements. The measured energy for each delivered pulse has been shown in black (associated with the left vertical axis), and the bending radius at each measurement has been shown in red (associated with the right vertical axis). For each repetition, the delivered energy was measured for one hour at half-circle, one hour at the long-term mBR, and 45 minutes below the long-term mBR.

the transmission efficiency and bending radius can be derived. Nevertheless, the transmission efficiency was estimated to be 2% less for the long-term mBR. This small change might be related to mode mixing (coupling to higher-order modes), which occurred because of microbends (imperfectly smooth core-cladding interface) [73]. Observing a higher output NA (approximately 0.1) can confirm the presence of mode mixing the bundle due to microbending. However, even such a small change in the transmitted energy can be calibrated based on feedback from the bending radius. Different sensing methodologies have been internally developed, capable of providing feedback on the bending radius [74–76].

By performing beam shaping in this work, as compared to other studies using similar fused-end fiber bundles [33–35], higher peak energy (102.6 mJ, as compared to 32 mJ/68 mJ) and peak power (20.52 MW, as compared to 6.4 MW/13.6 MW) was delivered through a fused-end fiber bundle with smaller active radius (1.5 mm as compared to 4 mm/2.5 mm) and smaller estimated long-term mBR (17.6 mm as compared to 34.3 mm/30.1 mm).

## 4. Conclusion

A fused-end bundle of 800 fibers with high flexibility was introduced to deliver high peak power Q-switched nanosecond Nd:YAG laser pulses at 532 nm. The fiber bundle was tested for more than 8 hours (approximately 30,000 pulses) at different bending radiuses, down to 15 mm. Given the low NA of the launch condition, the fiber bundle showed almost bend-insensitive behavior and was capable of delivering pulses with peak power of more than 20 MW (>100 mJ/5 ns), even at the defined long-term mBR. The maximum applicable peak power of the employed laser was tested in this study. The fiber bundle, however, has the potential to deliver higher peak power

Biomedical Optics EXPRESS

levels. Due to homogenizing the laser beam profile using a top-hat beam shaper, all the fibers in the bundle delivered the same energy level, providing high LIDT compared to that of the Gaussian beam. To the best of our knowledge, this is the most flexible fiber delivery system capable of delivering high peak power Q-switched laser pulses at 532 nm. The delivery system developed has the potential for use in flexiscopic applications.

## Funding

Werner Siemens Foundation through the Minimally Invasive Robot-Assisted Computer-guided LaserosteotomE (MIRACLE) project.

## Disclosures

The authors declare no conflicts of interest.

## References

1. L. M. B. Bernal, H. Abbasi, and A. Zam, "Laser in bone surgery," in *Lasers in Oral and Maxillofacial Surgery*, S. Stübinger, F. Klämpfl, M. Schmidt, and H. Zeilhofer, eds. (Springer, 2020), pp. 99–109.
2. K. Hyun Wook, L. Ho, C. Shaochen, and A. J. Welch, "Enhancement of bovine bone ablation assisted by a transparent liquid Layer on a target surface," IEEE J. Quantum Electron. **42**(7), 633–642 (2006).
3. A. Vogel, P. Schweiger, A. Frieser, M. N. Asiyo, and R. Birngruber, "Intraocular Nd:YAG laser surgery: laser-tissue interaction, damage range, and reduction of collateral effects," IEEE J. Quantum Electron. **26**(12), 2240–2260 (1990).
4. C. Duverney, H. Abbasi, L. M. Beltran Bernal, T. Stauber, J. G. Snedeker, P. C. Cattin, A. Zam, and G. Rauter, "Robot- and laser-assisted bio-sample preparation: development of an integrated, intuitive system," in *MESROB*, (Springer, 2020).
5. M. Bahreini, B. Ashrafkhani, and S. H. Tavassoli, "Discrimination of patients with diabetes mellitus and healthy subjects based on laser-induced breakdown spectroscopy of their fingernails," J. Biomed. Opt. **18**(10), 107006 (2013).
6. M. Bahreini, Z. Hosseinimakarem, and S. H. Tavassoli, "A study of association between fingernail elements and osteoporosis by laser-induced breakdown spectroscopy," J. Appl. Phys. **112**(5), 054701 (2012).
7. M. Nazeri, A. E. Majd, R. Massudi, S. H. Tavassoli, A. Mesbahinia, and H. Abbasi, "Laser-induced breakdown spectroscopy via the spatially resolved technique using non-gated detector," J. Russ. Laser Res. **37**(2), 164–171 (2016).
8. H. Abbasi, G. Rauter, R. Guzman, P. Cattin, and A. Zam, "Laser-induced breakdown spectroscopy as a potential tool for autocarbonization detection in laserosteotomy," J. Biomed. Opt. **23**(07), 1 (2018).
9. H. Abbasi, P. C. Cattin, and A. Zam, "A simple acoustic-based method for lens-to-sample distance adjustment in µLIBS," in *Photonics North*, (IEEE, 2020).
10. H. N. Kenhagho, I. Sugiarto, R. Guzman, P. Cattin, and A. Zam, "Contact-free crater depth monitoring using measured acoustic shock waves for smart laser surgery applications: preliminary result," in *2019 International Conference on Radar, Antenna, Microwave, Electronics, and Telecommunications (ICRAMET)*, 2019), 118–121.
11. H. Nguendon Kenhagho, G. Rauter, R. Guzman, P. C. Cattin, and A. Zam, Comparison of acoustic shock waves generated by micro and nanosecond lasers for a smart laser surgery system, *SPIE BiOS* (SPIE, 2018), Vol. 10484.
12. H. Nguendon Kenhagho, F. Canbaz, T. E. Gomez Alvarez-Arenas, R. Guzman, P. Cattin, and A. Zam, "Machine learning-based optoacoustic tissue classification method for laser osteotomes using an air-coupled transducer," Lasers in Surgery and Medicine (2020).
13. W. Xia, D. Piras, M. K. Singh, J. C. van Hespen, T. G. van Leeuwen, W. Steenbergen, and S. Manohar, "Design and evaluation of a laboratory prototype system for 3D photoacoustic full breast tomography," Biomed. Opt. Express **4**(11), 2555–2569 (2013).
14. M. Ai, W. Shu, T. Salcudean, R. Rohling, P. Abolmaesumi, and S. Tang, "Design of high energy laser pulse delivery in a multimode fiber for photoacoustic tomography," Opt. Express **25**(15), 17713–17726 (2017).
15. T. J. Stephens, M. J. Haste, D. P. Towers, M. J. Thomson, M. R. Taghizadeh, J. D. C. Jones, and D. P. Hand, "Fiber-optic delivery of high-peak-power Q-switched laser pulses for in-cylinder flow measurement," Appl. Opt. **42**(21), 4307–4314 (2003).
16. A. Mehrani, D. Dorranian, and E. Solati, "Properties of Au/ZnO nanocomposite prepared by laser irradiation of the mixture of individual colloids," J. Cluster Sci. **26**(5), 1743–1754 (2015).
17. A. G. Rad, H. Abbasi, and K. Golyari, "Fabrication and nonlinear refractive index measurement of colloidal silver nanoparticles," Int. J. Appl. Phys. Math. **2**, 135–139 (2012).
18. P. Nasiri, D. Doranian, and A. H. Sari, "Synthesis of Au/Si nanocomposite using laser ablation method," Opt. Laser Technol. **113**, 217–224 (2019).
19. T. Schmidt-Uhlig, P. Karlitschek, M. Yoda, Y. Sano, and G. Marowsky, "Laser shock processing with 20 MW laser pulses delivered by optical fibers," Eur. Phys. J.: Appl. Phys. **9**(3), 235–238 (2000).

Biomedical Optics EXPRESS


20. A. P. Yalin, M. DeFoort, B. Willson, Y. Matsuura, and M. Miyagi, "Use of hollow-core fibers to deliver nanosecond Nd:YAG laser pulses to form sparks in gases," Opt. Lett. **30**(16), 2083–2085 (2005).
21. C. Dumitrescu, P. Puzinauskas, S. Olcmen, S. G. Buckley, S. Joshi, and A. P. Yalin, "Fiber-optic spark delivery for gas-phase laser-induced breakdown spectroscopy," Appl. Spectrosc. **61**(12), 1338–1343 (2007).
22. H. Abbasi, L. M. Beltrán Bernal, A. Hamidi, A. Droneau, F. Canbaz, R. Guzman, S. L. Jacques, P. C. Cattin, and A. Zam, "Combined Nd:YAG and Er:YAG lasers for real-time closed-loop tissue-specific laser osteotomy," Biomed. Opt. Express **11**(4), 1790–1807 (2020).
23. H. Abbasi, G. Rauter, R. Guzman, P. Cattin, and A. Zam, Differentiation of femur bone from surrounding soft tissue using laser-induced breakdown spectroscopy as a feedback system for smart laserosteotomy, *SPIE Photonics Europe* (SPIE, 2018), Vol. 10685.
24. H. Abbasi, I. Sugiarto, G. Rauter, R. Guzman, P. Cattin, and A. Zam, "Pilot ex vivo study of laser-induced breakdown spectroscopy to detect bone dehydration: an approach for irrigation feedback in laserosteotomy," in *ICEECS*, 2018).
25. A. Vogel, S. Busch, and U. Parlitz, "Shock wave emission and cavitation bubble generation by picosecond and nanosecond optical breakdown in water," J. Acoust. Soc. Am. **100**(1), 148–165 (1996).
26. V. Rastogi, S. Chaurasia, and D. S. Munda, "Laser induced damage studies in borosilicate glass using nanosecond and sub nanosecond pulses," J. Non-Cryst. Solids **463**, 138–147 (2017).
27. Y. Matsuura, K. Hanamoto, S. Sato, and M. Miyagi, "Hollow-fiber delivery of high-power pulsed Nd:YAG laser light," Opt. Lett. **23**(23), 1858–1860 (1998).
28. S. Sato, H. Ashida, Y.-W. Shi, Y. Matsuura, and M. Miyagi, Hollow-waveguide-based transmission of a Q-switched Nd:YAG laser beam for biological tissue ablation, *BiOS '99 International Biomedical Optics Symposium* (SPIE, 1999), Vol. 3596.
29. S. Sato, H. Ashida, T. Arai, Y.-W. Shi, Y. Matsuura, and M. Miyagi, "Vacuum-cored hollow waveguide for transmission of high-energy, nanosecond Nd:YAG laser pulses and its application to biological tissue ablation," Opt. Lett. **25**(1), 49–51 (2000).
30. D. C. S. Beddows, O. Samek, M. Liška, and H. H. Telle, "Single-pulse laser-induced breakdown spectroscopy of samples submerged in water using a single-fibre light delivery system," Spectrochim. Acta, Part B **57**(9), 1461–1471 (2002).
31. X. -H. Zhao and Y. Gao, "Use of tapered fibers to deliver nanosecond laser pulses to launch flyer plates," in *International Summer Session: Lasers and Their Applications* (Optical Society of America, 2011), Th27.
32. 32. X. Fan and J. Liu, New simplified coupling system of 15MW Nd:YAG laser pulse with 600um optical fiber by use of a taper fiber, *AOMATT 2008 - 4th International Symposium on Advanced Optical Manufacturing* (SPIE, 2009), Vol. 7282.
33. A. Buehler, E. Herzog, D. Razansky, and V. Ntziachristos, "Video rate optoacoustic tomography of mouse kidney perfusion," Opt. Lett. **35**(14), 2475–2477 (2010).
34. D. Razansky, A. Buehler, and V. Ntziachristos, "Volumetric real-time multispectral optoacoustic tomography of biomarkers," Nat. Protoc. **6**(8), 1121–1129 (2011).
35. K. Sivasubramanian, V. Periyasamy, K. K. Wen, and M. Pramanik, "Optimizing light delivery through fiber bundle in photoacoustic imaging with clinical ultrasound system: Monte Carlo simulation and experimental validation," J. Biomed. Opt. **22**(4), 041008 (2017).
36. H. El-Rabii and G. Gaborel, "Laser ignition of flammable mixtures via a solid core optical fiber," Appl. Phys. B **87**(1), 139–144 (2007).
37. R. R. J. Maier, D. P. Hand, A. Kuhn, P. Blair, M. R. Taghizadeh, and J. D. C. Jones, "Fibre optic beam delivery of nano-second Nd:YAG laser pulses for micro-machining," *International Congress on Applications of Lasers & Electro-Optics* 1999, 204–218 (1999).
38. J. Wu, H. Yu, Y. Qiu, Z. Zhang, T. Liu, F. Xue, W. Yu, X. Li, and A. Qiu, "Plasma characteristics and element analysis of steels from a nuclear power plant based on fiber-optic laser-induced breakdown spectroscopy," J. Phys. D: Appl. Phys. **52**(1), 014006 (2019).
39. Y. Qiu, J. Wu, X. Li, T. Liu, F. Xue, Z. Yang, Z. Zhang, and H. Yu, "Parametric study of fiber-optic laser-induced breakdown spectroscopy for elemental analysis of Z3CN20-09M steel from nuclear power plants," Spectrochim. Acta, Part B **149**, 48–56 (2018).
40. A. Matsumoto, H. Ohba, M. Toshimitsu, K. Akaoka, A. Ruas, T. Sakka, and I. Wakaida, "Fiber-optic laser-induced breakdown spectroscopy of zirconium metal in air: Special features of the plasma produced by a long-pulse laser," Spectrochim. Acta, Part B **142**, 37–49 (2018).
41. S. Sasazawa, S. Kakino, and Y. Matsuura, "Optical-fiber-based laser-induced breakdown spectroscopy for detection of early caries," J. Biomed. Opt. **20**(6), 065002 (2015).
42. C. E. Dumitrescu, P. V. Puzinauskas, and S. Olcmen, "Movable fiber probe for gas-phase laser-induced breakdown spectroscopy," Appl. Opt. **47**(31), G88–G98 (2008).
43. Y. Matsuura, A. Tsuchiuchi, H. Noguchi, and M. Miyagi, "Hollow fiber optics with improved durability for high-peak-power pulses of Q-switched Nd:YAG lasers," Appl. Opt. **46**(8), 1279–1282 (2007).
44. Y. Matsuura, Y. Ozgur, and M. Miyagi, Bundled hollow-optical fiber for delivery of 30-MW peak power Nd:YAG laser pulses, *SPIE BiOS* (SPIE, 2006), Vol. 6083.
45. O. Yilmaz, M. Miyagi, and Y. Matsuura, "Bundled hollow optical fibers for transmission of high-peak-power Q-switched Nd:YAG laser pulses," Appl. Opt. **45**(27), 7174–7178 (2006).

Biomedical Optics EXPRESS


46. X. Xiao, "*Sensitive Quantification of Chlorine on Steel Surfaces Via Fiber-optic Laser-induced Breakdown Spectroscopy*," (The Pennsylvania State University, 2017).
47. Q. Zeng, L. Guo, X. Li, C. He, M. Shen, K. Li, J. Duan, X. Zeng, and Y. Lu, "Laser-induced breakdown spectroscopy using laser pulses delivered by optical fibers for analyzing Mn and Ti elements in pig iron," J. Anal. At. Spectrom. **30**(2), 403–409 (2015).
48. Q. Zeng, F. Deng, Z. Zhu, Y. Tang, B. Wang, Y. Xiao, L. Xiong, H. Yu, L. Guo, and X. Li, "Portable fiber-optic laser-induced breakdown spectroscopy system for the quantitative analysis of minor elements in steel," Plasma Sci. Technol. **21**(3), 034006 (2019).
49. T. Schmidt-Uhlig, P. Karlitschek, G. Marowsky, and Y. Sano, "New simplified coupling scheme for the delivery of 20 MW Nd:YAG laser pulses by large core optical fibers," Appl. Phys. B **72**(2), 183–186 (2001).
50. Y. Matsuura, G. Takada, T. Yamamoto, Y.-W. Shi, and M. Miyagi, "Hollow fibers for delivery of harmonic pulses of Q-switched Nd:YAG lasers," Appl. Opt. **41**(3), 442–445 (2002).
51. O. Yilmaz, Y. Matsuura, and M. Miyagi, "Delivery of 10-MW Nd:YAG laser pulses by bundled hollow fibers," in *2005 Pacific Rim Conference on Lasers & Electro-Optics*, (2005), 553–554.
52. J. Jia, H. Fu, Z. Hou, H. Wang, Z. Wang, F. Dong, Z. Ni, and Z. Zhang, "Effect of laser beam shaping on the determination of manganese and chromium elements in steel samples using laser-induced breakdown spectroscopy," Spectrochim. Acta, Part B **163**, 105747 (2020).
53. Z. Hou, M. S. Afgan, S. Sheta, J. Liu, and Z. Wang, "Plasma modulation effect of beam shaping to improve signal quality of laser induced breakdown spectroscopy," J. Anal. At. Spectrom. (2020).
54. A. V. Smith and B. T. Do, "Bulk and surface laser damage of silica by picosecond and nanosecond pulses at 1064 nm," Appl. Opt. **47**(26), 4812–4832 (2008).
55. M. Kimmel, B. Do, and A. Smith, Deterministic single shot and multiple shot bulk laser damage thresholds of borosilicate glass at 1.064 micron, *SPIE Laser Damage* (SPIE, 2011), Vol. 8190.
56. X. Sun, J. Li, A. Hokansson, D. Whelan, and M. Clancy, Study of laser-induced damage to large core silica fiber by Nd:YAG and Alexandrite lasers, *SPIE BiOS* (SPIE, 2009), Vol. 7173.
57. X. Sun and J. Li, Laser-induced damage to large core optical fiber by high peak power laser, *SPIE BiOS* (SPIE, 2013), Vol. 8576.
58. E. Specht, (2014), retrieved http://hydra.nat.uni-magdeburg.de/packing/cci/cci.html.
59. S. Kravitz, "Packing Cylinders into Cylindrical Containers," Mathematics Mag. **40**(2), 65–71 (1967).
60. N. Mladenović, F. Plastria, and D. Urošević, "Formulation space search for circle packing problems," in *International Workshop on Engineering Stochastic Local Search Algorithms*, (Springer, 2007), 212–216.
61. C. O. López and J. E. Beasley, "A heuristic for the circle packing problem with a variety of containers," Eur. J. Oper. Res. **214**(3), 512–525 (2011).
62. M. Niemz, "Threshold dependence of laser-induced optical breakdown on pulse duration," Appl. Phys. Lett. **66**(10), 1181–1183 (1995).
63. C. Carr, H. Radousky, and S. Demos, "Wavelength dependence of laser-induced damage: determining the damage initiation mechanisms," Phys. Rev. Lett. **91**(12), 127402 (2003).
64. W. Sellmeier, "Ueber die durch die Aetherschwingungen erregten Mitschwingungen der Körpertheilchen und deren Rückwirkung auf die ersteren, besonders zur Erklärung der Dispersion und ihrer Anomalien," Ann. Phys. **223**(11), 386–403 (1872).
65. I. H. Malitson, "Interspecimen comparison of the refractive index of fused silica," J. Opt. Soc. Am. **55**(10), 1205–1209 (1965).
66. J. W. Fleming and D. L. Wood, "Refractive index dispersion and related properties in fluorine doped silica," Appl. Opt. **22**(19), 3102–3104 (1983).
67. V. Brückner, Elements of optical networking: basics and practice of optical data communication; with 13 tables and 93 exercises (Vieweg+ Teubner, 2011).
68. H. Taylor, "Bending effects in optical fibers," J. Lightwave Technol. **2**(5), 617–628 (1984).
69. L. Yao, T. A. Birks, and J. C. Knight, "Low bend loss in tightly-bent fibers through adiabatic bend transitions," Opt. Express **17**(4), 2962–2967 (2009).
70. K. Naeem, Y. Kwon, Y. Chung, and I. Kwon, "Bend-loss-free distributed sensor based on Rayleigh backscattering in Ge-doped-core PCF," IEEE Sens. J. **18**(5), 1903–1910 (2018).
71. K. Iwai, H. Takaku, M. Miyagi, Y.-W. Shi, and Y. Matsuura, "Fabrication of shatter-proof metal hollow-core optical fibers for endoscopic mid-infrared laser applications," Fibers **6**(2), 24 (2018).
72. G. Mann and J. Krüger, Nanosecond laser damage of optical multimode fibers, *Pacific Rim Laser Damage 2016: Optical Materials for High Power Lasers* (SPIE, 2016), Vol. 9983.
73. L. Jeunhomme and J. P. Pocholle, "Mode coupling in a multimode optical fiber with microbends," Appl. Opt. **14**(10), 2400–2405 (1975).
74. S. Manavi, L. Witthauer, L. Iafolla, A. Zam, G. Rauter, and P. C. Cattin, "Temperature-compensated FBG-based 3D shape sensor using single-mode fibers," in *Advanced Photonics 2018 (BGPP, IPR, NP, NOMA, Sensors, Networks, SPPCom, SOF)*, OSA Technical Digest (online) (Optical Society of America, 2018), JTu6C.1.
75. L. Iafolla, L. Witthauer, A. Zam, G. Rauter, and P. C. Cattin, "Proof of principle of a novel angular sensor concept for tracking systems," Sens. Actuators, A **280**, 390–398 (2018).
76. L. Iafolla, L. Witthauer, S. Freund, L. Fasel, A. Zam, G. Rauter, and P. C. Cattin, "Preliminary Tests of the Miniaturization of a Novel Concept of Angular Sensors," in *2019 IEEE SENSORS*, 2019), 1–4.